Matter

CellPress

Article

Superionic amorphous $NaTaCl_6$ halide electrolyte for highly reversible all-solid-state Na-ion batteries

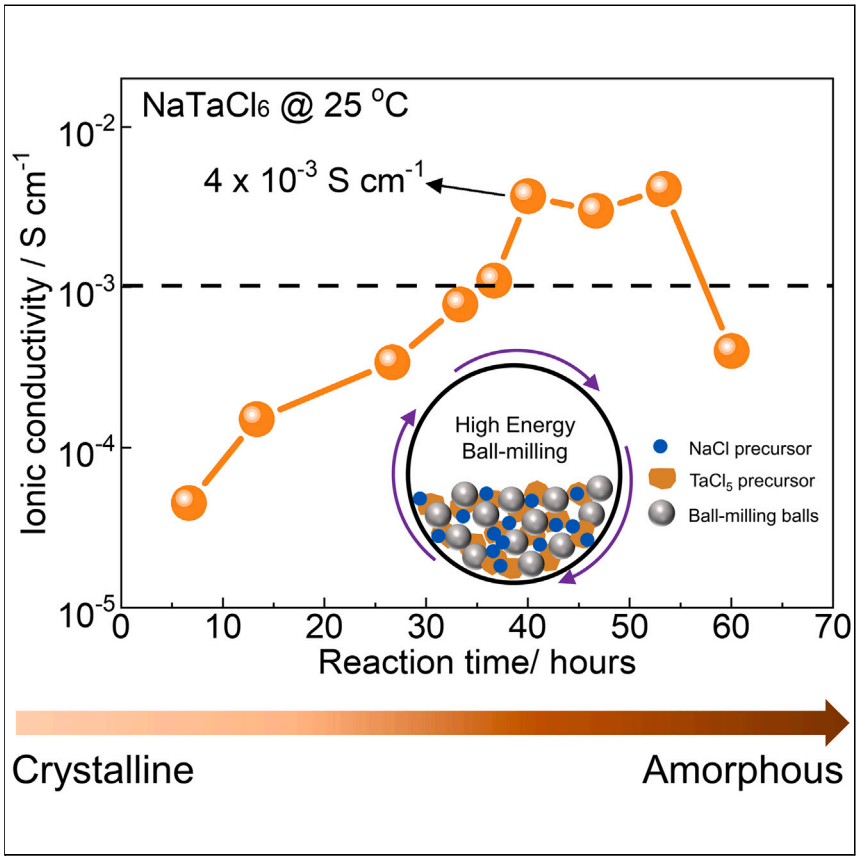

The exceptional electrochemical performance of all-solid-state Na-ion batteries is significantly enhanced by the development of amorphous Na-ion halide electrolytes with superhigh ionic conductivity (4 mS cm^{-1}).

Yang Hu, Jiamin Fu, Jiabin Xu, ..., Mingrui Yang, Yining Huang, Xueliang Sun

xsun9@uwo.ca

Highlights

Amorphous $NaTaCl_6$ halide electrolyte is synthesized via high-energy ball milling

A high Na-ion ionic conductivity of 4 mS cm^{-1} is achieved for halide electrolytes

Unique reconstructed local structures boost rapid Na-ion migration

Stable interfaces with high-voltage cathode enable superior battery performance

1 **Discovery**
A new material or phenomena

Hu et al., Matter 7, 1–17
March 6, 2024
https://doi.org/10.1016/j.matt.2023.12.017

Please cite this article in press as: Hu et al., Superionic amorphous $NaTaCl_6$ halide electrolyte for highly reversible all-solid-state Na-ion batteries, Matter (2023), https://doi.org/10.1016/j.matt.2023.12.017

Matter

CellPress

Article

Superionic amorphous $NaTaCl_6$ halide electrolyte for highly reversible all-solid-state Na-ion batteries

Yang Hu,[1] Jiamin Fu,[1,3] Jiabin Xu,[3] Jing Luo,[1] Feipeng Zhao,[1] Han Su,[1] Yu Liu,[1] Xiaoting Lin,[1] Weihan Li,[1] Jung Tae Kim,[1] Xiaoge Hao,[1] Xiaozhang Yao,[1] Yipeng Sun,[1] Jinjin Ma,[1] Haoqi Ren,[1] Mingrui Yang,[1] Yining Huang,[3] and Xueliang Sun[1,2,4,*]

SUMMARY

Designing Na-ion solid electrolytes (SEs) of high ionic conductivity and excellent chemical/mechanical compatibility with cathode materials remains challenging for all-solid-state Na-ion batteries (ASSNIBs). In this study, we successfully design and synthesize a novel amorphous $NaTaCl_6$ halide SE with unprecedented ionic conductivity of 4×10^{-3} S cm^{-1} at room temperature. The exceptional ionic conductivity arises from a unique reconstructed amorphous poly-($TaCl_6$) octahedra network with weakening Na-Cl interactions through high-energy mechanochemical reactions. Notably, the amorphous $NaTaCl_6$ halide SE exhibits remarkable mechanical deformability, chemical/electrochemical stability, and outstanding electrochemical performance when coupled with the $Na_3V_2(PO_4)_3$ cathode in ASSNIBs, resulting in a remarkable initial Coulombic efficiency of 99.60%, excellent rate performance (85% capacity retention at 2 C), and stable long-cycling profiles (81%/95%/98% capacity retention after 4,000/600/1,500 cycles at 3/1/0.5 C). This discovery of superionic amorphous Na-ion halide SEs opens a promising avenue for advancing high-performance ASSNIBs.

INTRODUCTION

Rechargeable Na-ion batteries (NIBs) have emerged as a highly promising alternative to Li-ion batteries due to the abundant Na resources in the Earth's crust (2.36% for Na compared to 0.0017% for Li) as well as the shared chemistry/electrochemistry characteristics of Na^+ ions with Li^+ ions.[1,2] Among various strategies, all-solid-state NIBs (ASSNIBs) have garnered significant research attention due to their improved energy density and enhanced safety during operation.[3–6] As the key component of ASSNIBs, ideal solid electrolytes (SEs) should meet three main criteria: fast Na-ion transportation ability (ionic conductivity >1 × 10^{-3} S cm^{-1}), excellent interfacial stability toward electrodes, and high deformability. However, no single Na-ion SE fulfills all of the requirements in the three main categories of inorganic SEs (oxide, sulfide, and halide based). Oxide-based Na-ion SEs have shown promising Na-ion conductivity, reaching levels as high as 4×10^{-3} S cm^{-1} through aliovalent or equivalent substitutions in NASICON structures ($Na_{3+x}M_yM'_{2-y}Si_{2-z}P_zO_{12}$, M or M′ = Zr, Ca, Mg, Zn, La, Ti, Nb). However, their inherent high mechanical stiffness results in significant interfacial resistance between the cathode and SEs, making them susceptible to cracks or mechanical failure during cycling.[7–12] For sulfide-based Na-ion SEs, exceptional ionic conductivity ranging from 2×10^{-4} S cm^{-1} to 3×10^{-2} S cm^{-1} has been

PROGRESS AND POTENTIAL

The depletion of finite fossil fuel resources has driven humanity's relentless pursuit of alternative clean energy storage solutions. Among various emerging candidates, Na-ion batteries (SIBs) have gained attention due to the abundant sodium element resources. A compelling approach to enhance the energy density of SIBs at the cell level involves incorporating Na-ion solid electrolytes (SEs) without separators in full cells. The key to achieving remarkable all-solid-state sodium-ion batteries (ASSNIBs) lies in the development of Na-ion superionic solid conductors. In this study, we synthesized a novel amorphous $NaTaCl_6$ halide SE tailored for ASSNIBs applications. With a remarkable ionic conductivity of 4×10^{-3} S cm^{-1} and exceptional interfacial stability with high-voltage Na-ion cathodes, this unique amorphous halide SE bestows ASSNIBs with exceptional performance metrics. These findings underscore its substantial implications for diverse applications.

achieved in Na_3PnX_4-type (Pn = P, Sb, W; X = S, Se) and $Na_{11}Sn_2PnX_{12}$-type (Pn = P, Sb; X = S, Se) structures.[13–19] Nevertheless, unlike their Li-ion counterparts, the absence of effective Na-ion coatings hinders the formation of favorable interfaces between sulfide SEs and typical layered oxide or polyanion-type cathodes in ASSNIBs, thus limiting their practical applications.[20–22] In comparison, although halide-based Na-ion SEs offer favorable mechanical flexibility and a broad electrochemical stability window, their limited Na-ion migration hampers practical use.[23–26] Thus far, the primary approach for enhancing ionic conductivity involves aliovalent substitution to adjust the concentration of Na-ion vacancies along the diffusion pathway, a common strategy derived from Li-ion halide SEs.[27–29] However, the reported highest ionic conductivity of Na-ion halide SEs (1.1×10^{-4} S cm^{-1} of $0.13ZrO_2$-0.61NaCl-$0.26Na_2ZrCl_6$) still falls short of meeting the threshold required for practical applications (>10^{-3} S cm^{-1}).[23,24,30,31] Consequently, there is an urgent need to develop efficient Na-ion conduction mechanisms tailored for Na-ion halide SEs.

The allure of amorphous SEs has captured considerable research focus, owing to their remarkable mechanical flexibility and potential for rapid ionic conduction due to the highly decoupled charge carriers from supporting matrix.[32,33] The exploration of amorphous sulfide and oxide SEs can be traced back to the 1980s, marked by the attainment of a noteworthy ionic conductivity of $\sim 10^{-3}$ S cm^{-1} within the Li_2S-P_2S_5-LiI ternary system.[34] Subsequently, Li_2S-P_2S_5/SiS_2/B_2S_3 and Li_2O-B_2O_3/P_2O_5 binary systems both were found to exhibit high ionic conductivity.[35–39] These systems exploit the dual roles of Li_2S/Li_2O as glass modifiers and P_2S_5/SiS_2/B_2S_3 as glass formers.[40] However, when using analogous strategies in the realm of Na-ion systems, the attainment of high ionic conductivity (>1×10^{-3} S cm^{-1}) remains an infrequent achievement. For instance, the Na_2O-B_2O_3-P_2O_5 ternary system and the Na_2S-P_2S_5 binary system yield ionic conductivities of only 3.5×10^{-10} and 1.43×10^{-5} S cm^{-1}, respectively.[41,42] This stark contrast in ionic conductivity between Na-ion and Li-ion counterparts underscores the pressing need for innovative mechanisms and novel designs in crafting amorphous structures, particularly tailored for Na-ion amorphous SEs.

In this study, we successfully achieved the first amorphous Na-ion halide SE via high-energy mechanochemical reactions, capitalizing on the brittle and two-dimensional characteristics of the $NaTaCl_6$ (NTC) structure. The resulting amorphous NTC SE exhibits an unprecedented ionic conductivity of 4×10^{-3} S cm^{-1} at room temperature (RT). Via various spectroscopy and thermodynamic analyses, the unique rapid Na-ion migration behavior within the reconstructed poly-($TaCl_6$) amorphous halide matrix is identified. The wide electrochemical window of amorphous NTC endows ASSNIBs with a remarkable initial Coulombic efficiency (ICE) of 99.60%, which surpasses all of the reported values in both Li-ion and Na-ion all-solid-state batteries, even exceeding the ICE observed in liquid cells.[43] Meanwhile, the fabricated ASSNIBs exhibit exceptional electrochemical performance at RT (85% capacity retention at 2 C rate, 98% capacity retention after 1,500 cycles at 0.5 C, 95% capacity retention after 600 cycles at 1 C). Notably, ASSNIBs can also deliver 81% capacity retention over 4,000 cycles with an average Coulombic efficiency of 99.96% at high temperature (60°C), indicating the excellent high-temperature tolerance of amorphous NTC. The exceptional ICE, excellent rate performance, and extraordinary cycling performance collectively suggest low mechanical interfacial resistance and an unprecedented level of chemical and electrochemical stability between amorphous NTC electrolyte and $Na_3V_2(PO_4)_3$ (NVP) cathode, underscoring its promising potential for practical applications in ASSNIBs.

[1]Department of Mechanical and Materials Engineering, University of Western Ontario, London, ON N6A 5B9, Canada

[2]Eastern Institute for Advanced Study, Eastern Institute of Technology, Ningbo, Zhejiang 3150200, P.R. China

[3]Department of Chemistry, University of Western Ontario, London, ON N6A 5B7, Canada

[4]Lead contact

*Correspondence: xsun9@uwo.ca

https://doi.org/10.1016/j.matt.2023.12.017

Please cite this article in press as: Hu et al., Superionic amorphous $NaTaCl_6$ halide electrolyte for highly reversible all-solid-state Na-ion batteries, Matter (2023), https://doi.org/10.1016/j.matt.2023.12.017

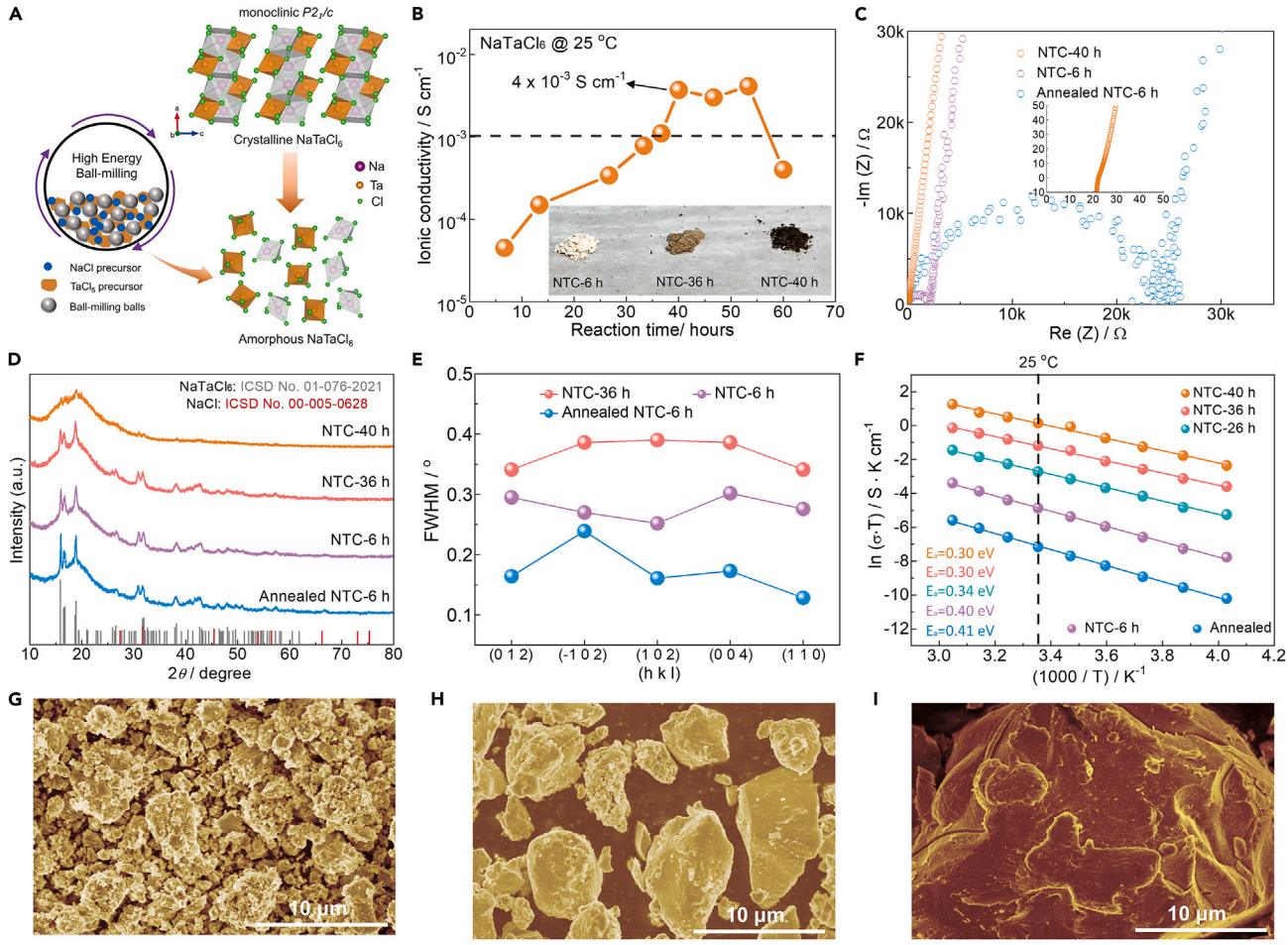

Figure 1. Synthesis of amorphous NTC halide electrolyte

(A) Schematic illustration of amorphization process of NTC halide electrolyte via high-energy ball milling.

(B) The relationship between obtained ionic conductivities of NTC at RT (25°C) and mechanochemical reaction time (inset: NTC powders with different reaction times).

(C and D) Nyquist plots (C) and (D) XRD patterns of various ball milled NTC and annealed NTC.

(E) The FWHM value of representative crystal planes in XRD patterns.

(F) Arrhenius conductivity plots of NTC with different ionic conductivities.

(G–I) SEM images of NTC powders with various reaction times: (G) 6 h, (H) 26 h, and (I) 40 h.

RESULTS AND DISCUSSION

Similar to reported Na_3YCl_6 (NYC; ICSD no. 04-015-3668), NTC (ICSD no. 01-076-2021) crystallizes in a monoclinic structure with the $P2_1/n$ space group, and Na^+ ions in NTC fully occupy the Wyckoff 4e sites. In comparison, Na^+ ions fully occupy both the Wyckoff 2d and 4e sites in NYC due to fewer Na^+ vacancies caused by the lower valence state of Y^{3+} (Figure S1). The lack of partial occupation of Na^+ ions in NTC and NYC makes them both poor Na-ion conductors. The crystallographic atom positions in NYC and NTC are provided in Tables S1 and S2. The structure of NTC displays a distinctive two-dimensional feature, with two NTC sheets aligned along the c-axis, as depicted in Figure 1A. Within NTC, Ta^{5+} ions form $TaCl_6$ octahedra coordinated by 6 Cl^- atoms, which share edges with 7-coordinated $NaCl_7$ face-capped octahedra. Notably, there are 6 inequivalent Cl^- sites in $TaCl_6$ octahedra, whereas only 3 inequivalent Cl^- sites exist in YCl_6 octahedra, indicating a higher distortion degree of $TaCl_6$ octahedral. Furthermore, the average interatomic

Please cite this article in press as: Hu et al., Superionic amorphous $NaTaCl_6$ halide electrolyte for highly reversible all-solid-state Na-ion batteries, Matter (2023), https://doi.org/10.1016/j.matt.2023.12.017

distance between Na^+ and Cl^- in NTC is 2.93 Å, surpassing the Na-Cl average distance of 2.85 Å observed in NYC, which indicates weaker binding between Na^+ and Cl^- ions in NTC. Under typical ball milling reaction time (5 h), Figure S2 demonstrates that NTC SE exhibits a 3-fold higher ionic conductivity ($\sim 10^{-5}$ S cm^{-1}) compared to the previously reported NYC structure ($\sim 10^{-8}$ S cm^{-1}).[30] This enhanced ionic conductivity can be attributed to the easier generation of defects and Na-ions vacancies in brittle NTC crystal structure during high-energy ball milling. In theory, the two-dimensional characteristic and highly distorted crystal structure of NTC render its long-range order susceptible to disruption during a high-energy ball milling process, potentially leading to complete amorphization with prolonged ball milling time as shown in Figure 1A. Considering the substantial ionic conductivities observed in reported amorphous SEs resulting from the efficient transport of decoupled charge carriers in an open amorphous supporting matrix, it is essential to correlate the phase transition of NTC SEs with the Na-ion transportation mechanism upon elongated mechanochemical reaction time.[44–46] NTC SEs were synthesized by the mechanochemical reaction of stoichiometric NaCl and $TaCl_5$ precursors. Figure 1B illustrates the evolution of ionic conductivities of NTC SEs at RT upon different reaction times, while maintaining other parameters unchanged (see experimental procedures section for details). Corresponding Nyquist plots for NTC SEs with varying reaction times are displayed in Figure S3. The ionic conductivity of NTC SEs initially increases from 6×10^{-5} to 4×10^{-3} S cm^{-1} at RT during the first 40 h of ball milling. In addition, it stabilizes at 3–4 $\times 10^{-3}$ S cm^{-1} from 40 h and up to 55 h and decreases below 10^{-3} S cm^{-1} after 60-h ball milling. The highest ionic conductivity of NTC (4×10^{-3} S cm^{-1} at RT) can be achieved after a 40-h reaction, and it is nearly 2 orders of magnitude higher than that of $Na_{2.25}Y_{0.25}Zr_{0.75}Cl_6$ SE, marking the highest value reported within the Na-ion halide electrolytes community thus far.[30] The inset in Figure 1B displays the morphological transition of NTC SEs with increasing ionic conductivities, evolving from white loose powder at an ionic conductivity of 10^{-5} S cm^{-1} to light gray compact powder at an ionic conductivity of 10^{-4} S cm^{-1}, ultimately transforming into dark loose and sticky powders at an ionic conductivity of 4×10^{-3} S cm^{-1}. The morphological transition with shape, consistency, and color change signifies the dynamic alterations in the local environment of NTC SEs with the extended duration of ball milling. The electronic conductivity of dark NTC SE at the highest ionic conductivity of 4×10^{-3} S cm^{-1}, as shown in Figure S4, is 1.25×10^{-9} S cm^{-1}, indicating that the high observed conductivity in Nyquist plots predominantly arises from Na-ion transportation rather than electron conduction behavior. To further demonstrate the importance of amorphous species for Na-ion conduction, the NTC SE sample obtained after typical 5-h reaction (6×10^{-5} S cm^{-1}) had undergone annealing treatment at 200°C for 2 h to improve its crystallinity. Figure 1C presents a comparison of Nyquist plots for three NTC SEs using the same blocking electrode configuration. The ionic conductivity of annealed sample decreases to $\sim 10^{-6}$ S cm^{-1}, one order of degree lower than the sample after a typical 6-h reaction (6×10^{-5} S cm^{-1}). Meanwhile, it is noteworthy that the annealed sample of NTC with a 40-h reaction time also demonstrates a decrease in ionic conductivity by three degrees (Figure S5). This significantly reduced ionic conductivity in the annealed sample further reinforces the scenario that NTC crystals exhibit poor ionic conducting ability and amorphous species formed during high-energy ball milling plays a crucial role in facilitating Na-ion conduction in NTC SEs. Figure 1D displays the corresponding X-ray diffraction (XRD) patterns of NTC SEs with representative reaction times (see the full XRD patterns in Figure S6). A small amount of NaCl impurity can be observed. The broader and weaker characteristic peaks observed in NTC samples with higher ionic conductivities suggest a higher amorphization degree, confirming the

Please cite this article in press as: Hu et al., Superionic amorphous $NaTaCl_6$ halide electrolyte for highly reversible all-solid-state Na-ion batteries, Matter (2023), https://doi.org/10.1016/j.matt.2023.12.017

amorphous-induced Na^+-ion conduction mechanism. The annealed NTC sample exhibits the sharpest and strongest peak, whereas the NTC sample after 40-h ball milling (the highest ionic conductivity of 4×10^{-3} S cm^{-1}) displays nearly disappearing characteristic peaks associated with NTC crystal planes. In Figure 1E, the full width at half-maximum (FWHM) values of five representative crystal planes in NTC are extracted from the XRD patterns depicted in Figure 1D. Because of the near-amorphous nature of the 40-h NTC sample, a comparison is made among NTC SEs after 3 different ball milling times: 36 h, 6 h, and an annealed 6-h sample. The FWHM values of five representative crystal planes consistently increase with the increase in ionic conductivity, further supporting the correlation between ionic conductivity and the degree of amorphization in NTC. Figure 1F presents the Arrhenius plots for NTC SEs with varying reaction times. The activation energies of NTC SEs exhibit a gradual decrease from 0.41 to 0.30 eV as the ionic conductivity increases, suggesting reduced migration energy barriers for Na^+ ions in NTC SEs with progressive amorphization process. The temperature-dependent Nyquist plots of five NTC SEs are depicted in Figure S7. Scanning electron microscopy (SEM) images provide the morphological evolution information of NTC SEs during high-energy mechanochemical reactions, as illustrated in Figures 1G–1I. In an NTC sample with a 6-h reaction time (the lowest ionic conductivity of 6×10^{-5} S cm^{-1}), a multitude of particles with sharp edges are observed due to its high crystallinity (high-resolution transmission electron microscopy [HRTEM] images in Figure S8). As the ball milling time increases to 40 h (ionic conductivity of 4×10^{-4} S cm^{-1}), NTC particles start to grow larger and tend toward a more uniform distribution due to the fusion of grain boundaries. Remarkably, in NTC samples with the longest ball milling time, large and uniformly shaped particles with an approximate diameter of 20 μm are discernible, correlated with the formed amorphous halide matrix. The observed trend in SEM images aligns with the phase transition from the crystalline to the amorphous state and the ionic conductivity evolution of NTC SEs.

Figure 2A illustrates the potential superionic Na^+-ion conducting amorphous structures in highly conductive NTC SEs. Through high-energy mechanochemical reactions, $TaCl_6$ octahedra approach one another and undergo significant distortion, leading to the formation of a poly-($TaCl_6$) backbone. Driven by electrostatic force, the closer arrangement of $TaCl_6$ octahedra repels Na^+ ions from their original positions to the amorphous poly-($TaCl_6$) halide matrix, facilitating rapid Na^+-ion migration. Various spectroscopic and thermodynamic analyses were conducted to identify the amorphous structure. X-ray absorption spectroscopy (XAS) was collected to investigate the local structure evolution of NTC SEs due to their intrinsic high sensitivity to the local coordination environment around specific elements.[47] Figure 2B presents Na K-edge spectra of NTC SEs, providing valuable information about the local environment evolution surrounding Na atoms. The observed pre-edge feature around the photon energy of 1,074 eV in both NaCl standard and NTC SEs corresponds to the parity forbidden transition from the Na *1s* core state to the *3s* state located at the bottom of the conduction band,[48] offering insights into the symmetry and electron configuration of the absorbing Na atom. In the case of the highly symmetrical NaCl crystal, the pre-edge peak in the NaCl spectrum exhibits the highest intensity. However, the pre-edge peak intensity in NTC SEs decreases as the ionic conductivity increases, suggesting higher distortion degree around Na atoms. Within the near-edge region of both NTC SEs and NaCl standards, three distinct absorption peaks, labeled a, b, and c, arise from electron dipole transitions from the core *1s* state to the splitting triply degenerate Na *3p* states of t_{2g} symmetry, which are induced by its interaction with Cl *3s* and *3p* states.[49] Comparing NTC SEs with NaCl standard, the increasing photon energy of peak a indicates weaker Na-Cl interactions in NTC SEs. In addition, with the increasing ionic conductivity in NTC

Please cite this article in press as: Hu et al., Superionic amorphous $NaTaCl_6$ halide electrolyte for highly reversible all-solid-state Na-ion batteries, Matter (2023), https://doi.org/10.1016/j.matt.2023.12.017

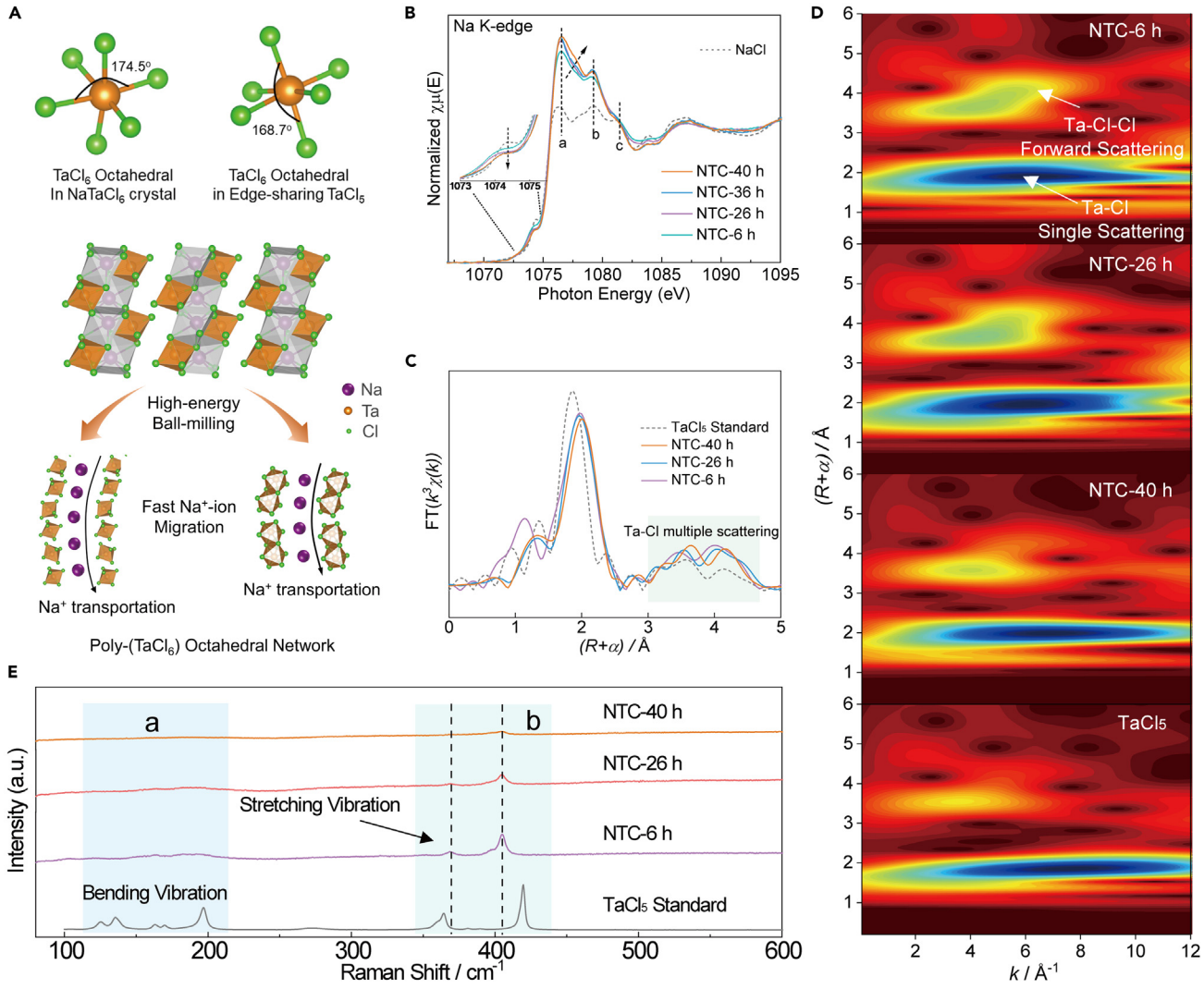

Figure 2. Na-ion conduction mechanism in amorphous NTC halide SE

(A) Schematic diagram for the Na-ion conduction mechanism in amorphous NTC and local structure distortion.

(B) Na K-edge XAS spectra for NTC with different ionic conductivities and NaCl standard.

(C) Fourier transform of Ta L_3-edge EXAFS in R space of NTC with different ionic conductivities and $TaCl_5$ standard before phase correction.

(D) wt of the k^2-weighted Ta L_3-edge EXAFS data.

(E) Raman spectra of $TaCl_5$ standard and NTC with various ionic conductivities.

SEs, the intensity of peak a increases, whereas the intensity of peak c decreases. These changes contribute to an overall sharper peak feature in the near-edge region of Na K-edge XAS. Theoretically, weaker interactions between Na and Cl atoms result in smaller splitting energies, leading to less spreading of the electronic transitions as well as more distinct and narrower features.[50] As shown in Figure 2B, the sharpest peak feature of NTC SE with the longest reaction time (40 h) indicates the weakest Na-Cl interactions, which correlates with the amorphous structure model presented in Figure 2A.

The local atomic structure evolution around Ta atoms in NTC SEs was further determined using Ta L_3-edge extended X-ray absorption fine structure (EXAFS) and X-ray absorption near-edge structure spectra. As shown in Figure S9, consistent white line features and absorption edge energy (E_0) values at Ta L_3-edge between NTC SEs

Please cite this article in press as: Hu et al., Superionic amorphous $NaTaCl_6$ halide electrolyte for highly reversible all-solid-state Na-ion batteries, Matter (2023), https://doi.org/10.1016/j.matt.2023.12.017

and $TaCl_5$ standard indicate unchanged oxidation states during the high-energy ball milling process. Fourier transformed (FT) k^2-weighted Ta L_3-edge EXAFS spectra without phase correction in the R space of $TaCl_5$ standards and NTC SEs are plotted in Figure 2C. The peaks observed at 1–3 Å can be attributed to single scattering from Cl^- coordination in the first shell. In comparison to the three main peaks (1.36 Å, 1.86 Å, and 2.39 Å) observed in $TaCl_5$, NTC SEs with short reaction times (6 h and 26 h) display a main peak at 1.98 Å, whereas an additional emerging peak appears at 1.33 Å in NTC SEs with ball milling times of 6 h and 40 h. Furthermore, compared to the NTC SE with a reaction time of 26 h, the main peak in the NTC SE with a long reaction time of 40 h shifts to higher distance. These observations indicate progressively distorted $TaCl_6$ octahedra with increasing ionic conductivity, aligning with the amorphous structure model shown in Figure 2A. It is important to note that the peak at 1.13 Å should be disregarded because it represents noise during Fourier transformation. Peaks observed at 3–5 Å in the R space are attributed to Ta–Na single scattering and Ta–Cl multiple scattering in the second shell, where the Ta–Cl multiple scattering exhibits more distinct characteristic peaks due to its higher degeneracy. The double-peak features of NTC SEs, as indicated by the green area in Figure 2C, gradually converge to $TaCl_5$ standard when ionic conductivity increases, suggesting increased distortion and proximity of $TaCl_6$ octahedra. Wavelet transformation (wt) of Ta L_3-edge EXAFS data provides more direct evidence for the gradual distorted $TaCl_6$ octahedra in NTC SEs. As depicted in Figure 2D, the multiple scattering region (as illustrated in the Feff modeling shown in Figure S10) exhibits a prominent signal for the Ta–Cl–Cl forward path in NTC, with a short reaction time of 6 h (the lowest ionic conductivity of 6×10^{-5} S cm^{-1}), which can be attributed to the nearly 180° Ta-Cl bond angle in NTC crystal as depicted in Figure 2A. However, the forward path signal is absent in the wt-EXAFS data of $TaCl_5$ standard due to a more distorted Ta-Cl bond. The signal of Ta–Cl–Cl forward path in NTC SEs weakens as the ionic conductivities increase and nearly vanish in NTC SE with the highest ionic conductivity (4×10^{-3} S cm^{-1}, 40 h), indicating the progressive distorted $TaCl_6$ octahedral in NTC SEs. Raman spectroscopy offers valuable insights into the microscopic vibration characteristics of $TaCl_6$ octahedra in NTC SEs. Figure 2E presents Raman spectra of three NTC SEs and $TaCl_5$ standard spectrum. The multiple peaks observed in region a and region b can be ascribed to the F_{2g} bending vibration and the A_{1g} stretching vibration of $TaCl_5$ dimer, respectively.[51] In comparison to the $TaCl_5$ standard spectrum, the two peaks at wavenumber of 360 and 420 cm^{-1}, which represent the A_{1g} stretching vibration of $TaCl_5$ dimer, converge in three NTC SEs, indicating the presence of separated $TaCl_6$ octahedra following the incorporation of Na-ions.[24,52] As the ionic conductivities increase, the NTC SEs exhibit broader A_{1g} stretching vibration characteristic peaks, indicating the decreased amount of separated $TaCl_6$ octahedra. Both F_{2g} bending vibration and A_{1g} stretching vibration peaks nearly disappear in the highly amorphous NTC SE, suggesting a complex vibration mode in the superionic Na^+-ion conducting amorphous structure.

Cl K-edge spectra are shown in Figures 3A and 3B to unveil the local structure evolution near Cl atoms. Regarding the near-edge and post-edge features, NTC SEs with low reaction times of 6 h and 26 h exhibit similarities with features b, d, and e observed in NaCl standard. However, NTC SEs with long reaction times of 36 h and 40 h resemble feature c observed in $TaCl_5$ standard with edge-sharing $TaCl_6$ octahedra. These observations signify that Na^+ ions are repulsed from the nearest-neighbor locations of Cl atoms, and $TaCl_6$ octahedra becomes closer as the ionic conductivity increases. However, it is important to note that the near-edge and post-edge features in NTC SEs with high ionic conductivity still differ from those of the $TaCl_5$ standard, indicating a more complex local environment surrounding Cl atoms

Please cite this article in press as: Hu et al., Superionic amorphous $NaTaCl_6$ halide electrolyte for highly reversible all-solid-state Na-ion batteries, Matter (2023), https://doi.org/10.1016/j.matt.2023.12.017

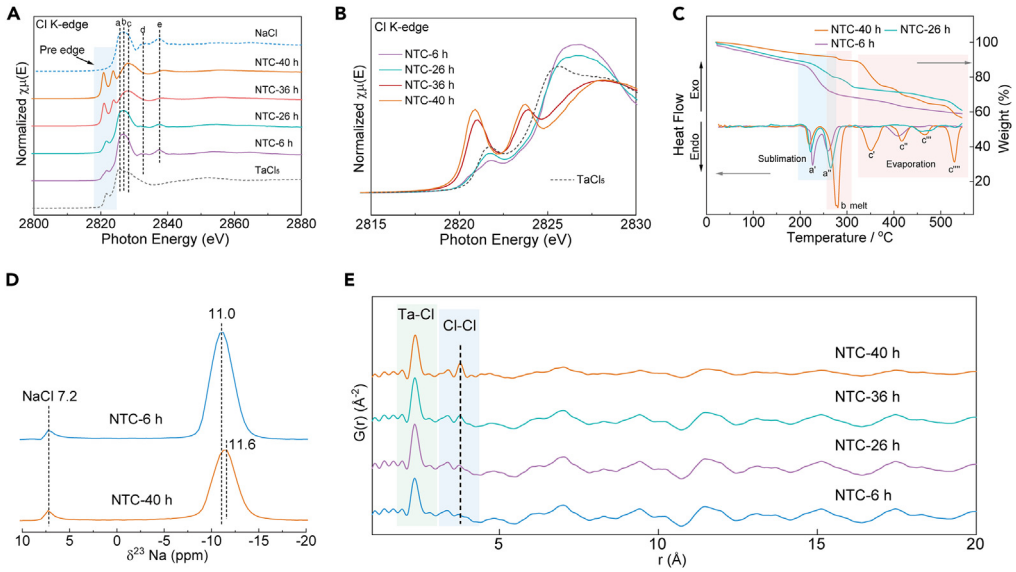

Figure 3. Characterization of disordered Na-ion superconducting structure in amorphous NTC SE

(A and B) XAS (A) and (B) pre-edge region of Cl K-edge XAS spectra for NTC with different ionic conductivities and $TaCl_5$/NaCl standards.

(C) TGA and DSC curves of NTC with different ionic conductivities.

(D) ^{23}Na MAS solid-state NMR spectra of crystalline and amorphous NTC.

(E) PDF of NTC with different ionic conductivities and $TaCl_5$ standard.

in superionic amorphous structure. Meanwhile, the pre-edge features of Cl K-edge XAS shown in Figure 3B are related to the transition from Cl *1s* orbitals to the mixing states of *3p* orbitals of Cl atoms and *5d* orbitals of Ta atoms, which can serve as an effective tool for probing the geometric properties and chemical bonding information around Cl atoms in NTC SEs. With increasing ionic conductivities, the pre-edge features of NTC SEs become more pronounced and split into two peaks, suggesting a gradual strengthening of orbital hybridization and significant splitting of unoccupied *3p-5d* hybridization orbitals. The evolution of pre-edge features arises from the progressively intense Ta–Cl interactions and distortion symmetry of $TaCl_6$ octahedral during elongated high-energy mechanochemical reactions, which correlates with the amorphous structure model presented in Figure 2A. It is noteworthy that the phase transition from crystalline to amorphous state involving partial rearrangement of the atomic structure can induce significant changes in the thermal properties of NTC SEs. In Figure 3C, thermal gravimetric analysis (TGA) and differential scanning calorimetry (DSC) curves of NTC SEs are presented spanning a temperature range from 25°C to 550°C, which can help establish a correlation between the changes in thermal properties and the local structural evolution in NTC SEs. All DSC curves have subtracted the background. Within the temperature range between 200°C and 300°C, multiple endothermic peaks are observed, indicating the sublimation or melting processes. After comparing with the TGA results, we find that NTC SEs with short reaction times of 6 h and 26 h (ionic conductivities of 6×10^{-5} and 4×10^{-4} S cm^{-1}) exhibit a noticeable weight loss of ~20% within the 200°C–300°C range. Therefore, we attribute peaks a and a′ to the sublimation of $TaCl_x$ species in these two samples, owing to the easily sublimable nature of $TaCl_x$ resulting from the high covalency of the Ta-Cl bonds. However, the NTC SE with a long reaction time (the highest ionic conductivity of 4×10^{-3} S cm^{-1}) exhibits limited weight loss in this region, suggesting that the strong endothermic peak b should be attributed to its melting process. It is noteworthy that the slight weight loss before 200°C is probably due to the absorption of moisture during transferring samples, which can

Please cite this article in press as: Hu et al., Superionic amorphous $NaTaCl_6$ halide electrolyte for highly reversible all-solid-state Na-ion batteries, Matter (2023), https://doi.org/10.1016/j.matt.2023.12.017

also be observed in the TGA and DSC curve of $TaCl_5$ precursor (Figure S11). Within the temperature range between 320°C and 550°C, all 3 samples exhibit multiple endothermic peaks accompanied by different amounts of weight loss. Notably, the NTC SE with the longest reaction time displays the highest number of endothermic peaks (c, c′, c″, c‴) and a significant weight loss of ~30%. These observations indicate a multistep evaporation process in highly amorphous NTC SE, which is a characteristic typical of amorphous materials. The endothermic peaks observed in the NTC SEs with reaction times of 6 h and 26 h within this temperature range can be attributed to the degradation process of SEs. Overall, the general thermal stability evolution trend is that the sublimation points of NTC SEs have increased along with longer ball milling time, and melting point is observed in the NTC SE with the longest reaction time (highest ionic conductivity). This enhanced thermal stability in the highly amorphous NTC SE is induced by the formation of stronger Ta-Cl bonds and an intertwined poly-($TaCl_6$) octahedra network through high-energy ball milling.

^{23}Na magic angle spinning (MAS) solid-state NMR spectra of NTC SEs provide more local structure information surrounding Na atoms, as shown in Figure 3D. The characteristic peak observed at 7.2 ppm in both spectra can be attributed to the NaCl impurity, whereas the peaks in the range of −10 to −12 ppm are associated with the local Na environment in NTC SEs. A spectra comparison between NTC SEs with short reaction time (6 h) and high reaction time (40 h) reveals that the broader characteristic peak in the high ionic conductivity sample exhibits a broader feature, suggesting a more disordered local Na environment.[53] According to the electron-shielding theory, the presence of electrons around a nucleus shields it from the full strength of an external magnetic field, resulting in a negative chemical shift observed in NMR spectra.[54] Therefore, the negative chemical shift observed in the high conductivity NTC SE (11.0–11.6 ppm) indicates an increasing number of Ta atoms with high electron density surrounding Na atoms, further proving the closer $TaCl_6$ octahedra in the poly-($TaCl_6$) network. Similar phenomena have been studied in systems such as $Na_{2.25}Y_{0.25}Zr_{0.75}Cl_6$ and $NaYF_4$.[30,55] Pair distribution function (PDF) analysis through FT-transformation of total scattering function can provide valuable information regarding the average distances between pairs of atoms in NTC SEs. As depicted in Figure 3E, the mid-range (5–20 Å) peak features exhibit gradually weakening characteristics, indicating more disordered structure with rising ionic conductivity. Notably, as the amorphization degree increases, a peak located at 3.5–4 Å, highlighted in the blue area of Figure 3E, becomes more prominent. This peak represents the gradually strengthening Cl-Cl scattering in NTC SEs, indicating a closer arrangement of $TaCl_6$ octahedra and the gradual formation of a superionic Na^+-ion conducting amorphous structure comprising a poly-($TaCl_6$) octahedral network. These findings are consistent with the results obtained from DSC, XAS, and ^{23}Na MAS solid-state NMR spectra.

To assess the practical application potential of amorphous NTC SE with ultra-high ionic conductivity, ASSNIBs were fabricated. Figure 4A initially presents the electrochemical window of amorphous NTC determined through linear sweep voltammetry (LSV) measurements. The cathodic limit is determined to be 4.0 V versus $Na_{15}Sn_4$, whereas the anodic limit is found to be 2.5 V versus $Na_{15}Sn_4$, resulting in a wide electrochemical window spanning from 2.5 to 4.0 V versus $Na_{15}Sn_4$. Due to the high anodic limit of amorphous NTC SE, *c*-Na_3PS_4 sulfide SE was introduced as protective layer for anode-electrolyte interfaces and the cell configuration of ASSNIBs can be seen in Figure S12. After careful evaluation, the NVP cathode with a typical NASICON structure was selected and coupled with amorphous NTC SE due to three reasons: (1) the high working voltage of 3.4 V versus $Na_{15}Sn_4$,[43] (2) the intrinsic flat charge-discharge plateau, and (3) the high chemical tolerance of poly-anion type cathodes with halide electrolytes.[56] As illustrated in Figure 4A, the dQ/dV curves of the NVP cathode exhibit two distinct sharp peaks at

Please cite this article in press as: Hu et al., Superionic amorphous $NaTaCl_6$ halide electrolyte for highly reversible all-solid-state Na-ion batteries, Matter (2023), https://doi.org/10.1016/j.matt.2023.12.017

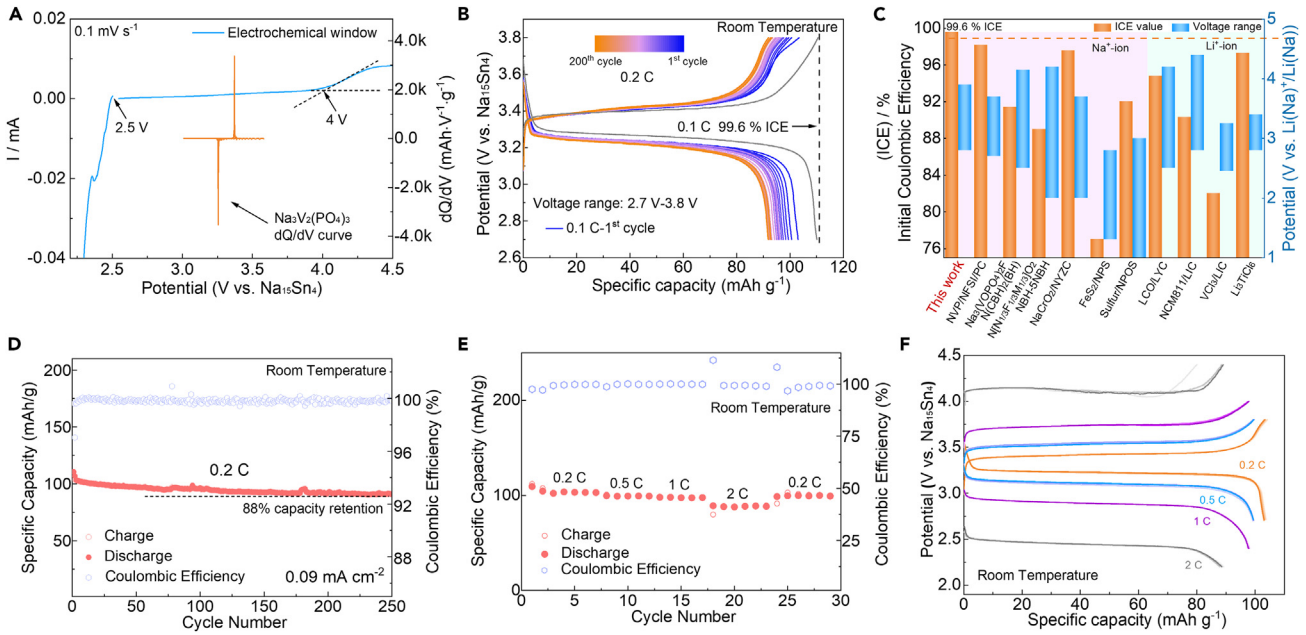

Figure 4. Electrochemical performance of full cells

(A) LSV profiles of amorphous NTC and dQ/dV curves of the NVP/NTC cathode composite.

(B) Representative galvanostatic charge-discharge curves of the NVP/NTC cathode composite during cycling under 0.2 C rate (the first cycle is under 0.1 C rate, 1 C = 118 mAh g^{-1}).

(C) The value of ICE in this work and representative cathode configuration in the reported literature.

(D) A 250 C profile of NVP/NTC cathode composite under 0.2 C rate.

(E) Rate performance of NVP/NTC cathode composite.

(F) Galvanostatic charge-discharge curves of the NVP/NTC cathode composite under different C rates.

3.25/3.4 V versus $Na_{15}Sn_4$ aligning within the electrochemical window of amorphous NTC SE, corresponding to the V^{3+}/V^{4+} redox couple. In Figure 4B, attributed to the high ionic conductivity (4×10^{-3} S cm^{-1} at RT) of amorphous NTC SE, the NVP cathode demonstrates an impressive discharge capacity of 110.6/102.5 mAh g^{-1} at 0.1/0.2 C and a low polarization of 150 mV (0.2 C) at RT. The galvanostatic charge-discharge curves of the NVP/NTC cathode composite exhibit consistent features without any plateau drop when tested under a low rate of 0.2 C over 200 cycles, indicating the well-preserved microstructure of the NVP cathode and the uninterrupted ionic percolation pathway during the charge-discharge process. Typical layered oxides, such as $LiNi_{0.8}Co_{0.1}Mn_{0.1}O_2$ and $NaCrO_2$, commonly undergo complicated structural changes and cathode-electrolyte interface forms during the initial charging process, resulting in unsatisfactory ICE. In comparison, the stable NASICON structure of NVP cathode enables fast and highly reversible migration of Na^+ ions within its covalent three-dimensional framework.[57–59] Impressively, the ICE value of the NVP/NTC cathode composite reaches 99.60% at a low current density of 0.1 C in this work, indicating the exceptional chemical and electrochemical compatibility between the NVP cathode and amorphous NTC SE, which represents the highest reported value among all-solid-state batteries, as summarized in Figure 4C.[25,43,60–67] The achieved 99.60% ICE value in ASSNIBs even surpasses the ICE value of 98.20% observed in liquid cells using the NVP cathode (NaFSI in propylene carbonate [PC]), demonstrating great promise for its practical applications.

Apart from the remarkable ICE value, the cycling and rate performance of the NVP/NTC cathode composite also demonstrate one of the best results among reported ASSNIBs. Figure 4D shows that under a low current density of 0.2 C, the NVP/NTC cathode

composite exhibits a high-capacity retention of 88% and maintains a high average Coulombic efficiency of 99.81% over 250 cycles at RT. The rate performance of the NVP/NTC cathode composite is depicted in Figure 4E, revealing that under 0.2/0.5/1/2 C, the output discharge capacity reaches 103.8/99.4/98.2/88.3 mAh g^{-1}, showcasing a high capacity retention of 85% even under 2 C, which represents the highest value among reported ASSNIBs (Table S3). The galvanostatic charge-discharge curves of NVP/NTC cathode composites under various current densities are shown in Figure 4F. The remaining flat plateaus under high current density indicate a dominant faradic electrochemical reaction during fast charge-discharge in ASSNIBs. It is noteworthy that the significant polarization observed under high current density can be attributed to the remarkably lower ionic conductivity of *c*-Na_3PS_4 (1×10^{-4} S cm^{-1} at RT) in comparison to the amorphous NTC SE used in this study. The Nyquist plot of *c*-Na_3PS_4 can be seen in Figure S13.

To discern the morphological evolution among the cathode composite powders, pre-cycled electrodes, and cycled electrodes, SEM images were collected. As depicted in Figure 5A, in contrast to the NVP cathode, which consists of regular spherical particles with an approximate diameter of 10 μm (Figure S14), the NVP/NTC composite exhibits significantly reduced particle size due to the ball milling mixing procedure, in which the amorphous NTC SE phase exhibits as a uniform coating layer on the surface of NVP cathode particles. The morphology of the uncycled electrode is illustrated in Figure 5B, revealing the presence of microcracks and areas where NVP cathode and amorphous NTC SE remain unconnected. After 100 cycles under 0.1 C, the electrode displays a highly uniform and homogeneous structure without microcracks as shown in Figure 5C. This transformation can be attributed to the continuous improvement of interfaces during the sodiation-desodiation process, resulting from the high deformability nature of the amorphous NTC SE. Long cycling tests were further conducted for the NVP/NTC cathode composite under both moderate and high current densities. Under a moderate current density of 0.5 C, the galvanostatic charge-discharge curves in Figure S15A almost overlap without voltage hysteresis, indicating its stable electrochemical behavior over cycling. Figure 5D demonstrates that the NVP/NTC cathode composite keeps 98% capacity retention over 1,500 cycles at RT. Under a high current density of 1 C, the galvanostatic charge-discharge curves of NVP/NTC cathode composite in Figure S15B exhibit an initial increase and stabilize at 95% of the highest discharge capacity after 600 cycles at RT, as shown in Figure 5E. The observed activation process under 1 C rate is attributed to the overall large resistance of fabricated ASSNIBs (Figure S16), caused by the low ionic conductivity of *c*-Na_3PS_4 (1×10^{-4} S cm^{-1} at RT). This issue can be addressed by designing novel SEs that are stable toward the $Na_{15}Sn_4$ anode and possess higher ionic conductivity in the future. The average Coulombic efficiency under 1 C rate reaches 99.98% over 600 cycles, indicating the highly reversible Na-ion intercalation/deintercalation in the NVP cathode facilitated by the superior interfacial compatibility between the NVP cathode and NTC SEs, which is further verified via electrochemical impedance spectroscopy (EIS) results (Figure S17). To the best of our knowledge, the RT cycling performance of the NVP/NTC cathode composite under both low and high current density represents the best result reported among all ASSNIBs (Table S3). High-temperature stability between the NVP cathode and NTC SEs as well as the battery performance were also studied at the elevated temperature (60°C). Remarkably, the elevated temperature efficiently addresses the low ionic conductivity of *c*-Na_3PS_4 and results in excellent rate performance up to 3 C rate. As depicted in Figure S15C, the NVP/NTC cathode composite exhibits a maximum value of 90.5 mAh g^{-1}, reaching 78% of the theoretical capacity of the NVP cathode. Furthermore, Figure 5F demonstrates the stable cycling profile of

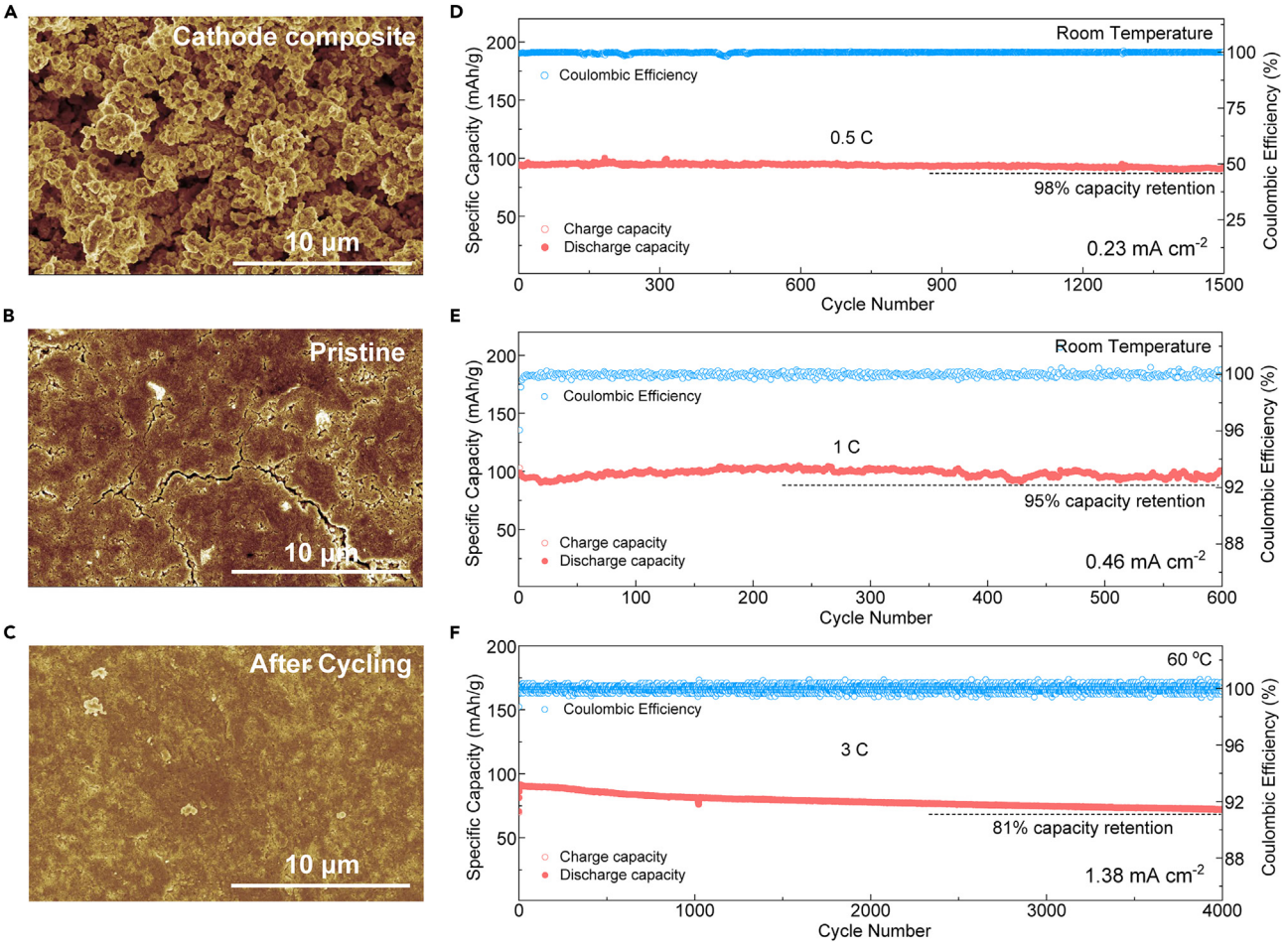

Figure 5. Long-term cycling performance of full cells

(A) SEM image of NVP/NTC cathode composite powder.

(B) SEM image of electrode before cycling.

(C) SEM image of electrode after 100 C.

(D) Long cycling profile of NVP/NTC cathode composite under 0.5 C rate at RT.

(E) Long cycling profile of NVP/NTC cathode composite under 1 C rate at RT.

(F) Long cycling profile of NVP/NTC cathode composite under 3 C rate at 60°C.

81% capacity retention, with a high average Coulombic efficiency of 99.96% over 4,000 cycles under 3 C rate. These results show that the NVP-NTC interface remains stable even at high temperatures, thus demonstrating its potential for safe application over a wide range of temperatures. The outstanding performance at different rates and operating temperatures can be attributed to the efficient Na-ion kinetics within the cathode composite, which is facilitated by the high RT ionic conductivity and amorphous nature of NTC SE in this work.

Conclusions

This study presents the design and synthesis of an amorphous NTC halide SE with remarkable properties, including high ionic conductivity, high deformability, and excellent chemical/electrochemical stability when paired with typical inorganic cathodes for ASSNIBs. The achieved record-high ionic conductivity of 4×10^{-3} S cm^{-1} at RT in amorphous NTC can be attributed to the weakened Na-Cl interactions and the formation of an amorphous poly-($TaCl_6$) octahedra network, facilitating fast migration of Na^+ ions

Please cite this article in press as: Hu et al., Superionic amorphous $NaTaCl_6$ halide electrolyte for highly reversible all-solid-state Na-ion batteries, Matter (2023), https://doi.org/10.1016/j.matt.2023.12.017

within the amorphous halide matrix. Notably, this study is the first to successfully couple a Na-ion halide electrolyte with a polyanion-type NVP cathode, and the integrated performance of the ASSNIBs reported here surpasses all of the previously reported results. The fabricated ASSNIBs exhibit impressive ICE values (99.60%), excellent rate performance (78%, 3 C), and long-cycling stability (81% at 4,000 cycles) at both RT and elevated temperature. The amorphous conduction mechanism proposed in this study opens up new possibilities for Na-ion halide electrolytes. For practical applications, incorporating more abundant elements such as Zr and Al into the glass network is necessary in the future. These findings provide insights into the development of novel Na-ion halide electrolytes and the understanding of Na-ion conduction mechanisms, thereby contributing to the advancement of high-performance ASSNIBs.

EXPERIMENTAL PROCEDURES

Resource availability

Lead contact

Further information and requests for resources should be directed to and will be fulfilled by the lead contact, Xueliang Sun (xsun9@uwo.ca).

Materials availability

All reagents are commercially available and were used as received. NaCl (99%), TaCl5 (99%), Na2S (99%) and P2S5 (99%) were purchased from Sigma-Aldrich. Carbon black was purchased from MSE supplies. Solid electrolytes reported in this work were synthesized using high-energy ball-milling machine (RETSCH Mill, PM200).

Data and code availability

All the data of this study are available within the main text and its supplemental information files.(Please link "supplemental information" to supp. information.)

Synthesis of SEs

NaCl (Sigma-Aldrich, 99%) and $TaCl_5$ (Sigma-Aldrich, 99%) were used as precursors and mixed manually in agate mortar according to the specific stoichiometric ratio. Then, the resulting powder (~1 g) was placed in a zirconia jar (100 mL) with 60-g zirconia balls in an Ar-filled glovebox (H_2O < 0.1 ppm, O_2 < 0.1 ppm). For every high energy ball milling cycle, a 10-min ball milling reaction at 600 rpm and a 5-min rest for natural cooling were applied. The resulting products were transferred to the glovebox for further use.

Na_2S (Sigma-Aldrich, 99%) and P_2S_5 (Sigma-Aldrich, 99%) were used as precursors and mixed manually in agate mortar according to the specific stoichiometric ratio. Then, the resulting powder (~1 g) was placed in a zirconia jar (100 mL) with 60-g zirconia balls in an Ar-filled glovebox (H_2O < 0.1 ppm, O_2 < 0.1 ppm). For every high-energy ball milling cycle, a 10-min ball milling reaction at 500 rpm and a 5-min rest for natural cooling were applied. The resulting powder was pressed into pellets and annealed for 2 h under 270°C to obtain the cubic Na_3PS_4 SE.

Characterizations

Lab-based XRD measurements were performed on a Bruker AXS D8 Advance with Cu Kα radiation (λ = 1.5406 Å). To prevent air exposure of air-sensitive samples, Kapton tape was used to cover the sample holder. Raman spectra were measured on a HORIBA Scientific LabRAM HR Raman spectrometer operated under laser beam at 532 nm. As-prepared halide electrolytes were attached on a carbon tape and covered by a transparent cover glass for the test. SEM images were obtained by using a Hitachi S-4800 field emission-scanning electron microscope (acceleration voltage 5 kV). HRTEM was performed in a double Cs-corrected transmission electron

Please cite this article in press as: Hu et al., Superionic amorphous $NaTaCl_6$ halide electrolyte for highly reversible all-solid-state Na-ion batteries, Matter (2023), https://doi.org/10.1016/j.matt.2023.12.017

microscope (Thermo Fisher Scientific Spectra Ultra) operated at 300 kV. TGA and DSC were carried out on an SDT Q600 (TA Instruments). The analysis was conducted by heating the sample from RT to 550°C at a rate of 10°C/min.

PDF of as-prepared halide electrolytes was collected using the Brockhouse X-ray Diffraction and Scattering (BXDS) beamlines at Canadian Light Source (CLS) with a wavelength of 0.2095 Å. The samples were loaded into 0.8-mm inner diameter polyimide capillaries and sealed with epoxy in an Ar-filled glovebox. XAS were collected from the hard X-ray microanalysis (HXMA), soft X-ray microcharacterization beamline (SXRMB), and spherical grating monochromator beamline (SGM) of CLS. For HXMA, the samples were mixed with an appropriate amount of boron nitride and then pressed into pellets. Al-plastic bags were applied for air-sensitive samples. For SXRMB and SGM, samples were spread on carbon tape and measured within a vacuum chamber. All of the XAS data were analyzed with Athena software.

^{23}Na solid-state NMR measurements were carried out on a Varian Infinity Plus wide-bore NMR spectrometer equipped with a 4.0-mm triple-tuned T3 MAS probe operating at the field strength of 9.4 T (ν_0 (^{23}Na) = 105.67 MHz). The ^{23}Na chemical shifts were referenced to a 1 M NaCl aqueous solution (0.04 ppm). ^{23}Na MAS solid-state NMR spectra were recorded using the spin echo sequence, a 90° pulse length of 5.7 μs, and a pulse delay of 2 s, with a spinning rate of 12 kHz.

Ionic and electronic conductivity test

The ionic conductivity of the SEs was measured using potentiostatic EIS on a German VMP3 multichannel potentiostation 3/Z, with a frequency range of 7 MHz to 1 Hz and a voltage amplitude of 10 mV. The electronic conductivity of SEs was determined through the direct current polarization method, with a voltage range from 0.1 to 0.5 V in increments of 0.1 V and a current response time of 60 min for each voltage step.

For the ionic and electronic conductivity test, the SE powders (~120 mg) were prepared by cold pressing into pellets (~0.7 mm thickness; 1 mm diameter) under ~400 MPa pressure with two stainless-steel rods as blocking electrode. To improve the contact between SE and stainless-steel rods, carbon black (~5 mg) was spread on both sides of the SE pellets and then pressed together under an ~200 MPa pressure.

LSV measurement

To evaluate the electrochemical window of amorphous NTC, LSV measurements were performed. First, approximately 100 mg of SE was cold pressed into a pellet to form a central layer. Second, a 10-mg mixture of SE and carbon black with a weight ratio of 70:30 was uniformly spread over one side of the pellet as working electrode. To prevent the severe side reaction between NTC layer and $Na_{15}Sn_4$ anode, 40 mg Na_3PS_4 was spread over the other side of the pellet. The LSV measurements were conducted using a versatile multichannel potentiostat 3/Z (VMP3), with a positive scan range from open-circuit voltage (OCV) to 6 V and a negative scan range from OCV to 0 V, at a scan rate of 0.1 mV s^{-1}.

Prepare of cathode composites and anodes

NVP cathode (Shenzhen Kejing Co.), NTC electrolyte, and carbon black were initially weighted according to the mass ratio of 4:4:2. The measured mixture (~500 mg in total) was placed in a zirconia jar (100 mL) with 30-g zirconia balls in an Ar-filled glovebox (H_2O < 0.1 ppm, O_2 < 0.1 ppm) and ball milled for 4 h under 200 rpm. The resulting cathode composite was transferred to the glovebox for further use.

Na metal (Sigma-Aldrich, 99%) and Sn powder (Sigma-Aldrich, 99%) were weighted according to the stoichiometric ratio. The resulting mixture was pressed several times in the Ar-filled glovebox to form homogeneous $Na_{15}Sn_4$ anode.

Fabrication of ASSNIBs

First, a polytetrafluoroethylene die with a 10-mm diameter was used to press 120 mg of NTC SE at ~250 MPa for 2 min, forming a central SE layer. Second, 10 mg of NVP/NTC cathode composite and 40 mg of Na_3PS_4 SSE were spread over both sides of NTC central layer uniformly and pressed together at ~500 MPa for another 3 min. Lastly, the $Na_{15}Sn_4$ powder was spread on the side of Na_3PS_4 uniformly and pressed together at ~250 MPa for 1 min. The galvanostatic charge-discharge test was performed on the Land test system (CT2001A, China). All of the electrochemical tests of ASSNIBs were carried out under a stack pressure of ~200 MPa.

SUPPLEMENTAL INFORMATION

Supplemental information can be found online at https://doi.org/10.1016/j.matt.2023.12.017.

ACKNOWLEDGMENTS

The authors are grateful for the support from the Natural Sciences and Engineering Research Council of Canada (NSERC), the Canada Research Chair Program (CRC), and the Canada Foundation for Innovation (CFI). The synchrotron-related characterizations were completed at the HXMA, SXRMB, and BXDS beamline in CLS, which is supported by the CFI, the NSERC, the National Research Council (NRC), the Canadian Institutes of Health Research (CIHR), the Government of Saskatchewan, and the University of Saskatchewan. Electron microscopy was performed at the Canadian Centre for Electron Microscopy (also supported by NSERC and other government agencies).

AUTHOR CONTRIBUTIONS

Y.H. and X.S. conceived the idea for the study. Y.H. collected the experimental data and wrote the raw manuscript. Y.H. and J.F. analyzed the data and discussed the project. X.L., J.X., J.L., J.T.K., Y.L., W.L., F.Z., H.S., X.H., H.R., and M.Y. participated in some discussions and data collection. J.X. and Y.H. carried out the solid-state NMR test. X.S. supervised the whole project.

DECLARATION OF INTERESTS

The authors declare no competing interests.

Received: August 23, 2023
Revised: November 5, 2023
Accepted: December 12, 2023
Published: January 12, 2024

REFERENCES

1. Yabuuchi, N., Kubota, K., Dahbi, M., and Komaba, S. (2014). Research development on sodium-ion batteries. Chem. Rev. *114*, 11636–11682.

2. Hwang, J.-Y., Myung, S.-T., and Sun, Y.-K. (2017). Sodium-ion batteries: present and future. Chem. Soc. Rev. *46*, 3529–3614.

3. Yang, H.-L., Zhang, B.-W., Konstantinov, K., Wang, Y.-X., Liu, H.-K., and Dou, S.-X. (2021). Progress and challenges for all-solid-state sodium batteries. Adv. Energy and Sustain. Res. *2*, 2000057.

4. Fan, S., Lei, M., Wu, H., Hu, J., Yin, C., Liang, T., and Li, C. (2020). A Na-rich fluorinated sulfate anti-perovskite with dual doping as solid electrolyte for Na metal solid state batteries. Energy Storage Mater. *31*, 87–94.

5. Li, C., Gu, L., and Maier, J. (2012). Enhancement of the Li conductivity in LiF by introducing glass/crystal interfaces. Adv. Funct. Mater. *22*, 1145–1149.

6. Hu, J., Yao, Z., Chen, K., and Li, C. (2020). High-conductivity open framework fluorinated electrolyte bonded by solidified ionic liquid wires for solid-state Li metal batteries. Energy Storage Mater. *28*, 37–46.

7. Hou, M., Liang, F., Chen, K., Dai, Y., and Xue, D. (2020). Challenges and perspectives of

NASICON-type solid electrolytes for all-solid-state lithium batteries. Nanotechnology *31*, 132003.

8. Yao, Y.-F.Y., and Kummer, J. (1967). Ion exchange properties of and rates of ionic diffusion in beta-alumina. J. Inorg. Nucl. Chem. *29*, 2453–2475.

9. Jian, Z., Hu, Y.S., Ji, X., and Chen, W. (2017). Nasicon-structured materials for energy storage. Adv. Mater. *29*, 1601925.

10. Goodenough, J.B., Hong, H.-P., and Kafalas, J. (1976). Fast Na^+-ion transport in skeleton structures. Mater. Res. Bull. *11*, 203–220.

11. Lu, Y., Alonso, J.A., Yi, Q., Lu, L., Wang, Z.L., and Sun, C. (2019). A high-performance monolithic solid-state sodium battery with Ca^{2+} doped $Na_3Zr_2Si_2PO_{12}$ electrolyte. Adv. Energy Mater. *9*, 1901205.

12. Ma, Q., Guin, M., Naqash, S., Tsai, C.-L., Tietz, F., and Guillon, O. (2016). Scandium-substituted $Na_3Zr_2(SiO_4)_2(PO_4)$ prepared by a solution-assisted solid-state reaction method as sodium-ion conductors. Chem. Mater. *28*, 4821–4828.

13. Jia, H., Peng, L., Yu, C., Dong, L., Cheng, S., and Xie, J. (2021). Chalcogenide-based inorganic sodium solid electrolytes. J. Mater. Chem. A *9*, 5134–5148.

14. Zhang, Z., Ramos, E., Lalère, F., Assoud, A., Kaup, K., Hartman, P., and Nazar, L.F. (2018). $Na_{11}Sn_2PS_{12}$: a new solid state sodium superionic conductor. Energy Environ. Sci. *11*, 87–93.

15. Hayashi, A., Noi, K., Sakuda, A., and Tatsumisago, M. (2012). Superionic glass-ceramic electrolytes for room-temperature rechargeable sodium batteries. Nat. Commun. *3*, 856.

16. Hayashi, A., Sakuda, A., and Tatsumisago, M. (2016). Development of sulfide solid electrolytes and interface formation processes for bulk-type all-solid-state Li and Na batteries. Front. Energy Res. *4*, 25.

17. Park, K.H., Bai, Q., Kim, D.H., Oh, D.Y., Zhu, Y., Mo, Y., and Jung, Y.S. (2018). Design strategies, practical considerations, and new solution processes of sulfide solid electrolytes for all-solid-state batteries. Adv. Energy Mater. *8*, 1800035.

18. Fuchs, T., Culver, S.P., Till, P., and Zeier, W.G. (2019). Defect-mediated conductivity enhancements in $Na_{3-x}Pn_{1-x}W_xS_4$ (Pn= P, Sb) using aliovalent substitutions. ACS Energy Lett. *5*, 146–151.

19. Hayashi, A., Masuzawa, N., Yubuchi, S., Tsuji, F., Hotehama, C., Sakuda, A., and Tatsumisago, M. (2019). A sodium-ion sulfide solid electrolyte with unprecedented conductivity at room temperature. Nat. Commun. *10*, 5266.

20. Kim, J.J., Yoon, K., Park, I., and Kang, K. (2017). Progress in the development of sodium-ion solid electrolytes. Small Methods *1*, 1700219.

21. Zhao, C., Liu, L., Qi, X., Lu, Y., Wu, F., Zhao, J., Yu, Y., Hu, Y.S., and Chen, L. (2018). Solid-state sodium batteries. Adv. Energy Mater. *8*, 1703012.

22. Wang, T., Yu, N., Qian, M., Feng, J., Cao, S., Yin, J., and Zhang, Q. (2018). Electrode materials for sodium-ion batteries: considerations on crystal structures and sodium storage mechanisms. Cancer Cell Int. *18*, 200–237.

23. Schlem, R., Banik, A., Eckardt, M., Zobel, M., and Zeier, W.G. (2020). $Na_{3-x}Er_{1-x}Zr_xCl_6$—A Halide-Based Fast Sodium-Ion Conductor with Vacancy-Driven Ionic Transport. ACS Appl. Energy Mater. *3*, 10164–10173.

24. Kwak, H., Lyoo, J., Park, J., Han, Y., Asakura, R., Remhof, A., Battaglia, C., Kim, H., Hong, S.-T., and Jung, Y.S. (2021). Na_2ZrCl_6 enabling highly stable 3 V all-solid-state Na-ion batteries. Energy Storage Mater. *37*, 47–54.

25. Asano, T., Sakai, A., Ouchi, S., Sakaida, M., Miyazaki, A., and Hasegawa, S. (2018). Solid halide electrolytes with high lithium-ion conductivity for application in 4 V class bulk-type all-solid-state batteries. Adv. Mater. *30*, 1803075.

26. Li, X., Liang, J., Yang, X., Adair, K.R., Wang, C., Zhao, F., and Sun, X. (2020). Progress and perspectives on halide lithium conductors for all-solid-state lithium batteries. Energy Environ. Sci. *13*, 1429–1461.

27. Li, X., Liang, J., Luo, J., Norouzi Banis, M., Wang, C., Li, W., Deng, S., Yu, C., Zhao, F., Hu, Y., et al. (2019). Air-stable Li_3InCl_6 electrolyte with high voltage compatibility for all-solid-state batteries. Energy Environ. Sci. *12*, 2665–2671.

28. Liang, J., Li, X., Wang, S., Adair, K.R., Li, W., Zhao, Y., Wang, C., Hu, Y., Zhang, L., Zhao, S., et al. (2020). Site-occupation-tuned superionic Li_xScCl_{3+x} halide solid electrolytes for all-solid-state batteries. J. Am. Chem. Soc. *142*, 7012–7022.

29. Fu, J., Wang, S., Liang, J., Alahakoon, S.H., Wu, D., Luo, J., Duan, H., Zhang, S., Zhao, F., Li, W., et al. (2023). Superionic Conducting Halide Frameworks Enabled by Interface-Bonded Halides. J. Am. Chem. Soc. *145*, 2183–2194.

30. Wu, E.A., Banerjee, S., Tang, H., Richardson, P.M., Doux, J.-M., Qi, J., Zhu, Z., Grenier, A., Li, Y., Zhao, E., et al. (2021). A stable cathode-solid electrolyte composite for high-voltage, long-cycle-life solid-state sodium-ion batteries. Nat. Commun. *12*, 1256.

31. Kwak, H., Kim, J.-S., Han, D., Kim, J.S., Park, J., Kwon, G., Bak, S.-M., Heo, U., Park, C., Lee, H.-W., et al. (2023). Boosting the interfacial superionic conduction of halide solid electrolytes for all-solid-state batteries. Nat. Commun. *14*, 2459.

32. Souquet, J.L. (1981). Ionic transport in amorphous solid electrolytes. Annu. Rev. Mater. Sci. *11*, 211–231.

33. Angell, C.A. (1992). Mobile ions in amorphous solids. Annu. Rev. Phys. Chem. *43*, 693–717.

34. Ujiie, S., Hayashi, A., and Tatsumisago, M. (2012). Structure, ionic conductivity and electrochemical stability of Li2S–P2S5–LiI glass and glass–ceramic electrolytes. Solid State Ionics *211*, 42–45.

35. Hayashi, A., Hama, S., Morimoto, H., Tatsumisago, M., and Minami, T. (2001). Preparation of Li2S–P2S5 amorphous solid electrolytes by mechanical milling. J. Am. Ceram. Soc. *84*, 477–479.

36. Morimoto, H., Yamashita, H., TATSUMISAGO, M., and MINAMI, T. (2000). Mechanochemical synthesis of the high lithium ion conductive amorphous materials in the systems Li2S-SiS2 and Li2S-SiS2-Li4SiO4. J. Ceram. Soc. Japan *108*, 128–131.

37. Estournès, C., Owens, A., Ménétrier, M., Levasseur, A., Rao, K., and Elliott, S. (1994). A structural study of Li2S- B2S3 glasses by neutron diffraction. J. Non-Cryst. Solids *171*, 80–86.

38. Ganguli, M., Bhat, M.H., and Raol, K. (1999). Lithium ion transport in Li_2SO_4–Li_2O–B_2O_3 glasses. Phys. Chem. Glasses *40*, 297–304.

39. Money, B.K., and Hariharan, K. (2009). Crystallization kinetics and phase transformation in superionic lithium metaphosphate (Li2O–P2O5) glass system. J. Phys. Condens. Matter *21*, 115102.

40. Kato, A., Nose, M., Yamamoto, M., Sakuda, A., Hayashi, A., and Tatsumisago, M. (2018). Mechanical properties of sulfide glasses in all-solid-state batteries. J. Ceram. Soc. Japan *126*, 719–727.

41. Sdiri, N., Elhouichet, H., Elakermi, E., Dhifallah, A., and Ferid, M. (2015). Structural investigation of amorphous Na_2O–P_2O_5–B_2O_3 correlated with its ionic conductivity. J. Non-Cryst. Solids *409*, 34–42.

42. Kumar Jha, P., Pandey, O.P., and Singh, K. (2013). Na2S-P2S5 Based Super-Ionic Glasses for Solid Electrolytes. Trans. Indian Ceram. Soc. *72*, 5–9.

43. Jian, Z., Han, W., Lu, X., Yang, H., Hu, Y.S., Zhou, J., Zhou, Z., Li, J., Chen, W., Chen, D., and Chen, L. (2013). Superior electrochemical performance and storage mechanism of $Na_3V_2(PO_4)_3$ cathode for room-temperature sodium-ion batteries. Adv. Energy Mater. *3*, 156–160.

44. Mizuno, F., Hayashi, A., Tadanaga, K., and Tatsumisago, M. (2005). New, highly ion-conductive crystals precipitated from Li_2S–P_2S_5 glasses. Adv. Mater. *17*, 918–921.

45. Kozen, A.C., Pearse, A.J., Lin, C.-F., Noked, M., and Rubloff, G.W. (2015). Atomic layer deposition of the solid electrolyte LiPON. Chem. Mater. *27*, 5324–5331.

46. Zhang, S., Zhao, F., Chen, J., Fu, J., Luo, J., Alahakoon, S.H., Chang, L.-Y., Feng, R., Shakouri, M., Liang, J., et al. (2023). A family of oxychloride amorphous solid electrolytes for long-cycling all-solid-state lithium batteries. Nat. Commun. *14*, 3780.

47. Yano, J., and Yachandra, V.K. (2009). X-ray absorption spectroscopy. Photosynth. Res. *102*, 241–254.

48. Murata, T., Matsukawa, T., and Naoe, S. (1988). XANES and EXAFS studies on K-shell absorption in $K_{1-x}Na_xCl$ solid solutions. Solid State Commun. *66*, 787–790.

49. McIntosh, G.J., and Chan, A. (2018). Probing hydrogen bonding interactions and impurity intercalation in gibbsite using experimental and theoretical XANES spectroscopy. Phys. Chem. Chem. Phys. *20*, 24033–24044.

50. Frati, F., Hunault, M.O.J.Y., and de Groot, F.M.F. (2020). Oxygen K-edge X-ray absorption spectra. Chem. Rev. *120*, 4056–4110.

51. Carlson, G.L. (1963). Vibrational spectra of some MCl_5 molecules: $SbCl_5$, PCl_5, $TaCl_5$ and $NbCl_5$. Spectrochim. Acta *19*, 1291–1307.

52. Kwak, H., Han, D., Lyoo, J., Park, J., Jung, S.H., Han, Y., Kwon, G., Kim, H., Hong, S.T., Nam, K.W., and Jung, Y.S. (2021). New cost-effective halide solid electrolytes for all-solid-state batteries: mechanochemically prepared Fe^{3+}-substituted Li_2ZrCl_6. Adv. Energy Mater. *11*, 2003190.

53. Duer, M.J. (2004). Introduction to Solid-State NMR Spectroscopy.

54. Jameson, C.J. (1996). Understanding NMR chemical shifts. Annu. Rev. Phys. Chem. *47*, 135–169.

55. Arnold, A.A., Terskikh, V., Li, Q.Y., Naccache, R., Marcotte, I., and Capobianco, J.A. (2013). Structure of $NaYF_4$ upconverting nanoparticles: a multinuclear solid-state NMR and DFT computational study. J. Phys. Chem. C *117*, 25733–25741.

56. Cronk, A., Chen, Y.-T., Deysher, G., Ham, S.-Y., Yang, H., Ridley, P., Sayahpour, B., Nguyen, L.H.B., Oh, J.A.S., Jang, J., et al. (2023). Overcoming the Interfacial Challenges of Inorganic All-Solid-State Batteries. ACS Energy Lett. *8*, 827–835.

57. Guo, S., Li, Q., Liu, P., Chen, M., and Zhou, H. (2017). Environmentally stable interface of layered oxide cathodes for sodium-ion batteries. Nat. Commun. *8*, 135.

58. Li, X., Gao, A., Tang, Z., Meng, F., Shang, T., Guo, S., Ding, J., Luo, Y., Xiao, D., Wang, X., et al. (2021). Robust Surface Reconstruction Induced by Subsurface Ni/Li Antisites in Ni-Rich Cathodes. Adv. Funct. Mater. *31*, 2010291.

59. Streich, D., Erk, C., Guéguen, A., Müller, P., Chesneau, F.-F., and Berg, E.J. (2017). Operando monitoring of early Ni-mediated surface reconstruction in layered lithiated Ni–Co–Mn oxides. J. Phys. Chem. C *121*, 13481–13486.

60. Jin, M., Cheng, S., Yang, Z., Luo, Y., and Guo, Y. (2023). A novel high-voltage solid electrolyte of $Na_3B_{24}H_{23}$ for 4 V all-solid-state sodium battery. Chem. Eng. J. *455*, 140904.

61. Asakura, R., Reber, D., Duchêne, L., Payandeh, S., Remhof, A., Hagemann, H., and Battaglia, C. (2020). 4 V room-temperature all-solid-state sodium battery enabled by a passivating cathode/hydroborate solid electrolyte interface. Energy Environ. Sci. *13*, 5048–5058.

62. Chi, X., Zhang, Y., Hao, F., Kmiec, S., Dong, H., Xu, R., Zhao, K., Ai, Q., Terlier, T., Wang, L., et al. (2022). An electrochemically stable homogeneous glassy electrolyte formed at room temperature for all-solid-state sodium batteries. Nat. Commun. *13*, 2854.

63. Liang, J., Li, X., Kim, J.T., Hao, X., Duan, H., Li, R., and Sun, X. (2023). Halide Layer Cathodes for Compatible and Fast-Charged Halides-Based All-Solid-State Li Metal Batteries. Angew. Chem. Int. Ed. *62*, e202217081.

64. Wang, K., Gu, Z., Xi, Z., Hu, L., and Ma, C. (2023). Li_3TiCl_6 as ionic conductive and compressible positive electrode active material for all-solid-state lithium-based batteries. Nat. Commun. *14*, 1396.

65. Wan, H., Mwizerwa, J.P., Qi, X., Xu, X., Li, H., Zhang, Q., Cai, L., Hu, Y.-S., and Yao, X. (2018). Nanoscaled Na3PS4 solid electrolyte for all-solid-state FeS2/Na batteries with ultrahigh initial coulombic efficiency of 95% and excellent cyclic performances. ACS Appl. Mater. Interfaces *10*, 12300–12304.

66. Wang, K., Ren, Q., Gu, Z., Duan, C., Wang, J., Zhu, F., Fu, Y., Hao, J., Zhu, J., He, L., et al. (2021). A cost-effective and humidity-tolerant chloride solid electrolyte for lithium batteries. Nat. Commun. *12*, 4410.

67. Liu, J., Wang, Z., Lu, Z., Zhang, L., Xie, F., Vasileff, A., and Qiao, S.-Z. (2019). Efficient surface modulation of single-crystalline $Na_2Ti_3O_7$ nanotube arrays with Ti^{3+} self-doping toward superior sodium storage. ACS Mater. Lett. *1*, 389–398.